

# Design principles for oxygen-reduction activity on perovskite oxide catalysts for fuel cells and metal-air batteries

Jin Suntivich<sup>1</sup>, Hubert A. Gasteiger<sup>2†\*</sup>, Naoaki Yabuuchi<sup>2</sup>, Haruyuki Nakanishi<sup>3</sup>, John B. Goodenough<sup>4</sup> and Yang Shao-Horn<sup>1,2\*</sup>

**The prohibitive cost and scarcity of the noble-metal catalysts needed for catalysing the oxygen reduction reaction (ORR) in fuel cells and metal-air batteries limit the commercialization of these clean-energy technologies. Identifying a catalyst design principle that links material properties to the catalytic activity can accelerate the search for highly active and abundant transition-metal-oxide catalysts to replace platinum. Here, we demonstrate that the ORR activity for oxide catalysts primarily correlates to  $\sigma^*$ -orbital ( $e_g$ ) occupation and the extent of B-site transition-metal-oxygen covalency, which serves as a secondary activity descriptor. Our findings reflect the critical influences of the  $\sigma^*$  orbital and metal-oxygen covalency on the competition between  $O_2^{2-}/OH^-$  displacement and  $OH^-$  regeneration on surface transition-metal ions as the rate-limiting steps of the ORR, and thus highlight the importance of electronic structure in controlling oxide catalytic activity.**

Driven by growing concerns about global warming and the depletion of petroleum resources, developing renewable energy production and storage technologies represents one of the major scientific challenges of the twenty-first century. A critical element in the pursuit of this quest is the discovery of efficient and cost-effective catalysts for use in electrochemical energy conversion processes<sup>1,2</sup> such as the oxygen evolution reaction (OER) and oxygen reduction reaction (ORR), both of which are central to the efficiencies of direct-solar<sup>3</sup> and electrolytic water-splitting<sup>4,5</sup> devices, fuel cells<sup>6</sup> and metal-air batteries<sup>7,8</sup>. Although Sabatier's principle provides a qualitative argument for tuning catalytic activity by varying the bond strength between the catalyst surface and the reactant/product (neither too strong nor too weak, leading to maximum activity at moderate bond strength), it has no predictive power to find catalysts with enhanced activity. Recent *ab initio*<sup>9</sup> and experimental studies<sup>10,11</sup> have identified a unique catalyst property ('activity descriptor') that governs the strength of the metal-oxygen bond and the ORR activity of platinum-based metals in acid ( $O_2 + 4H^+ + 4e^- \rightarrow 2H_2O$ ). Controlling the ORR activity descriptor—the *d*-band centre relative to the Fermi level<sup>9,12</sup>—has quantitatively led to the discovery of promising new platinum-based catalysts for ORR in proton exchange membrane fuel cells (PEMFCs)<sup>10,13</sup>.

Alkaline fuel cells and metal-air batteries, which use transition-metal oxides for catalysing the ORR ( $O_2 + 2H_2O + 4e^- \rightarrow 4OH^-$ ), offer an alternative solution to PEMFCs. Oxides have shown reasonably high activity for the ORR in fuel cells<sup>14,15</sup> and the OER in water electrolysis<sup>5,16</sup> and direct solar water splitting<sup>17</sup> at neutral and high values of pH. However, a lack of fundamental understanding of the ORR mechanism and the material properties that govern

catalytic activity hampers the development of highly active oxide catalysts. In this Article, we report a volcano relationship between a material property that serves as the activity descriptor and the intrinsic ORR activity of perovskite-based oxides. Such information has predictive power and provides insights into the design of new catalysts with enhanced ORR activity similar to those reported for platinum-based metals<sup>10,11,13</sup>.

We take advantage of the flexibility of the physical-chemical and catalytic properties of the perovskite family, where A sites with rare-earth metal ions and B sites with transition-metal ions can allow partial substitution to form  $AA'B'B'O_3$  (Fig. 1a) to experimentally examine a large number of oxides (15 total) to establish a catalytic descriptor for ORR. Matsumoto *et al.*<sup>18–20</sup> and Bockris and Otagawa<sup>21</sup> have reported geometric currents of perovskites in thick, porous electrodes as a function of potential, but the intrinsic specific ORR activity (kinetic current densities normalized to catalyst surface area) necessary for ORR mechanistic discussion is not available. We have recently reported a methodology using a thin-film rotating-disk electrode with well-defined oxygen transport<sup>15</sup> to allow a precise comparison of the ORR activities of different transition-metal oxides. This method yields a more accurate determination of the intrinsic ORR activity than that estimated from the data reported by Bockris and Otagawa<sup>15</sup>, as oxygen mass transport resistances in thin-film electrodes are much better compensated than thick electrodes with very high internal surface area. In this Article, we apply this methodology to assess the ORR activity of 15 perovskite-based oxides with various A-site ( $La_{1-x}Ca_xBO_3$ ,  $La_{1+x}BO_{3+x}$ ) and B-site ( $LaB_{1-x}B'_xO_3$ ) substitutions, which is used to identify the material properties (descriptors) that govern their intrinsic ORR activities. Here we use the molecular-orbital approach

<sup>1</sup>Materials Science and Engineering Department and Electrochemical Energy Laboratory, Massachusetts Institute of Technology, 31-056, 77 Massachusetts Avenue, Cambridge, Massachusetts 02139, USA, <sup>2</sup>Mechanical Engineering Department and Electrochemical Energy Laboratory, Massachusetts Institute of Technology, 31-056, 77 Massachusetts Avenue, Cambridge, Massachusetts 02139, USA, <sup>3</sup>Fuel Cell System Development Division, Toyota Motor Corporation, Higashifuji Technical Center 1200, Mishuku, Susono, Shizuoka 410-1193, Japan, <sup>4</sup>Texas Materials Institute, University of Texas at Austin, ETC 9.184, Austin, Texas 78712, USA; <sup>†</sup>Present address: Department of Chemistry, Technische Universität München, Lichtenbergstrasse 4, D-85747 Garching, Germany. \*e-mail: hubert.gasteiger@tum.de; shaohorn@mit.edu

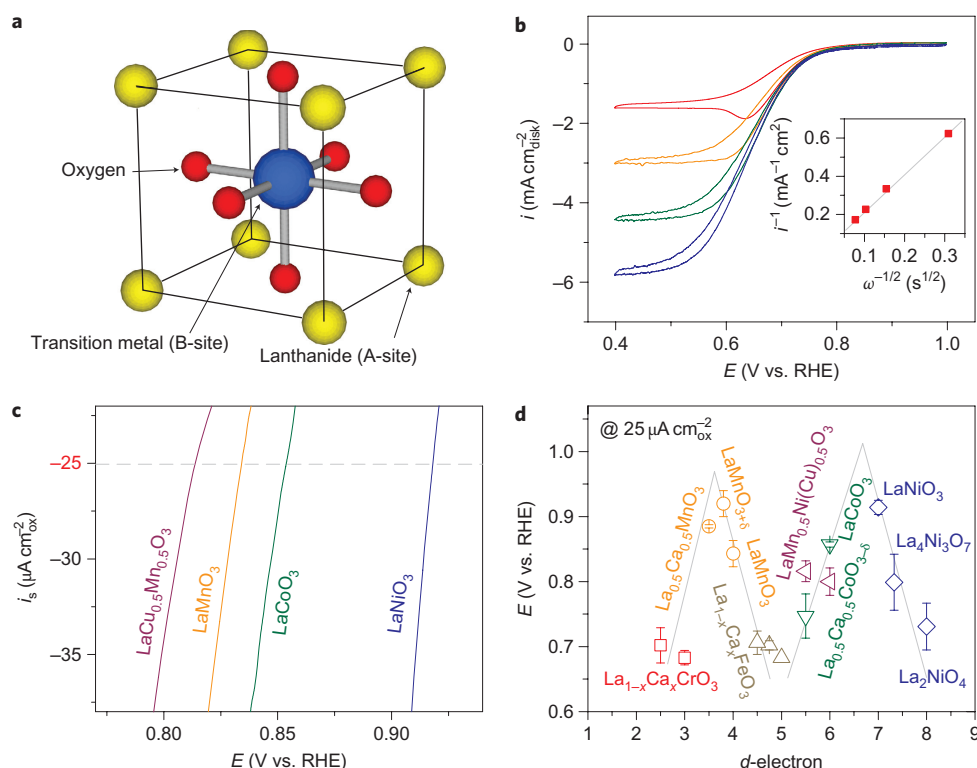


**Figure 1 | ORR activity of perovskite transition-metal-oxide catalysts.** **a**,  $ABO_3$  perovskite structure. **b**, Oxygen reduction activity of  $LaCu_{0.5}Mn_{0.5}O_3$  electrode in  $O_2$ -saturated 0.1 M KOH at 10  $mV s^{-1}$  scan rate and rotation rates of 100, 400, 900 and 1,600 r.p.m. The Koutecky-Levich analysis (inset) of the limiting currents (0.4 V) indicates a  $4e^-$  transfer reaction. **c**, Specific activities of  $LaCu_{0.5}Mn_{0.5}O_3$ ,  $LaMnO_3$ ,  $LaCoO_3$  and  $LaNiO_3$ . The potential at  $25 \mu A cm_{ox}^{-2}$  is used as a benchmark for comparison (shown as the intersection between the activity and the horizontal grey dashed line). **d**, Potentials at  $25 \mu A cm_{ox}^{-2}$  of the perovskite oxides have an M-shaped relationship with  $d$ -electron number. Data symbols vary with type of B ions (Cr, red; Mn, orange; Fe, grey; Co, green; Ni, blue; mixed compounds, purple), where  $x = 0$  and 0.5 for Cr, and 0, 0.25 and 0.5 for Fe. Error bars represent standard deviations of at least three measurements.

to identify descriptors for the ORR activity of oxides, in contrast to the hypothesis proposed previously by Matsumoto *et al.*<sup>18–20</sup>, which is based on the conjecture that the ORR activity of oxide electrodes can be greatly influenced by the formation and filling of a  $\sigma^*$  band between the  $e_g$  orbital of bulk transition-metal ions and a molecular orbital of surface oxygen. The application of the molecular-orbital approach to these perovskites is supported by a large number of reports that the surface of transition-metal oxides favours electron localization over the bulk itinerant electron state<sup>22–24</sup>. Herein, we show that the primary descriptor that governs the ORR activity of the 15 perovskites examined in this work is the extent of  $\sigma^*$ -antibonding ( $e_g$ ) orbital filling of surface transition-metal ions. This hypothesis is further supported by increasing ORR activity with greater hybridization of the B–O (B-site-metal and oxygen) bond, as revealed by O K-edge X-ray absorption spectroscopy (XAS) analysis.

### ORR activity measurement of perovskites

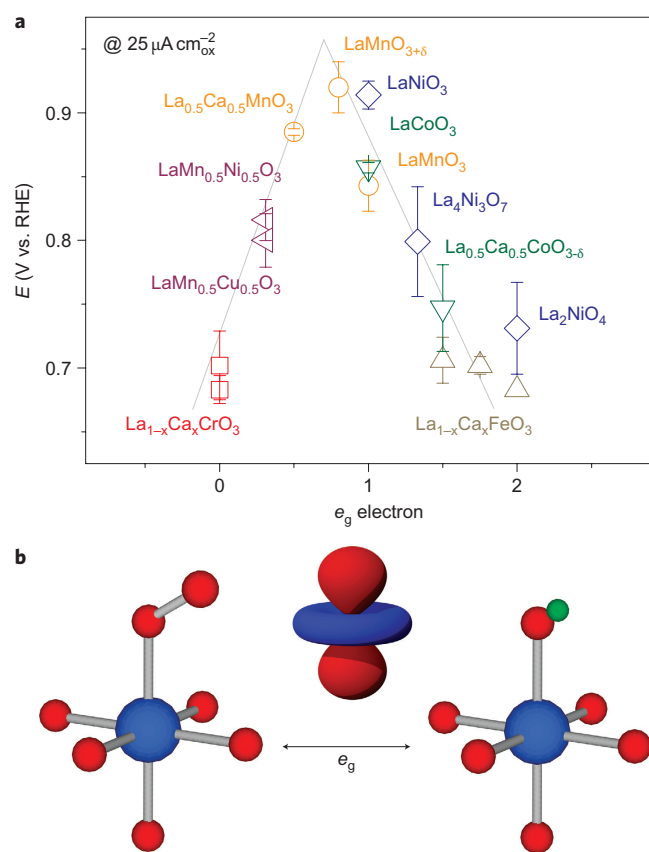
The ORR currents of a  $LaCu_{0.5}Mn_{0.5}O_3$  thin-film electrode at various rotation speeds are shown in Fig. 1b, as an example. The onset of the ORR occurs at  $\sim 0.8$  V versus RHE (reversible hydrogen electrode), and an oxygen-transport-limited current appears at potentials below  $\sim 0.5$  V versus RHE. The slope of the Koutecky-Levich plot in the mass-transport-limited region (0.4 V versus RHE, Fig. 1b inset) has a value of  $\sim 11 mA^{-1} cm_{disk}^2 s^{-1/2}$ , which indicates a  $4e^-$  reduction of oxygen to water<sup>15,25</sup>. The mass-transport correction to the oxygen diffusion overpotential was applied to all measurements to obtain the ORR kinetic currents as outlined in our previous work<sup>15</sup>. The surface-area-normalized kinetic current densities of four representative oxides, termed specific activity  $i_s$  (ref. 15), are plotted as a function of voltage in

Fig. 1c. Because all 15 oxide catalysts had comparable Tafel slopes of  $\sim 60$  mV per decade (Supplementary Fig. S1), the dashed line in Fig. 1c shows that the intrinsic activity for each catalyst can be assessed by the potential to achieve a given specific ORR current ( $25 \mu A cm_{ox}^{-2}$ ). For  $LaCu_{0.5}Mn_{0.5}O_3$ ,  $LaMnO_3$ ,  $LaCoO_3$  and  $LaNiO_3$ , this specific activity current can be reached at potentials of  $781(\pm 15)$ ,  $834(\pm 24)$ ,  $847(\pm 3)$  and  $908(\pm 8)$  mV versus RHE, respectively. A higher potential indicates higher electrocatalytic activity for a given oxide. It is interesting to note that oxides such as  $LaMnO_{3+\delta}$  and  $LaNiO_3$  have intrinsic ORR activity comparable to state-of-the-art Pt/C (Supplementary Fig. S2).

### ORR activity descriptor identification

To identify an ORR activity descriptor, we begin by examining the relationship between the  $3d$ -electron number of B-site ions and ORR activity with the hypothesis that the  $3d$ -electron number, which represents the antibonding electron occupation of the B–O bond, can influence B– $O_2$  interaction strength<sup>16</sup> (Supplementary Scheme S1). This hypothesis is supported by the recent observation that the adsorption energy trend of B– $O_2$  can be approximated by that of B–O (ref. 26). Interestingly, the comparison between the ORR activity of the perovskites and the  $d$ -electron number per B cation (Fig. 1d) reveals an M-shaped relationship with the maximum activity attained near  $d^4$  and  $d^7$ , which resembles the trend reported for the oxidation activity of gas-phase CO and hydrocarbon on perovskites<sup>27,28</sup>.

We further show that the intrinsic ORR activity of all the oxides exhibits a volcano shape as a function of the  $e_g$ -filling of B ions. Assuming that the  $O_2$  molecule probably adsorbs on the surface B sites end-on (Fig. 2b), the  $e_g$  orbital directed towards an  $O_2$



**Figure 2 | Role of  $e_g$  electron on ORR activity of perovskite oxides.**

**a**, Potentials at  $25 \mu\text{A cm}^{-2}$  as a function of  $e_g$  orbital in perovskite-based oxides. Data symbols vary with type of B ions (Cr, red; Mn, orange; Fe, grey; Co, green; Ni, blue; mixed compounds, purple), where  $x = 0$  and  $0.5$  for Cr, and  $0$ ,  $0.25$  and  $0.5$  for Fe. Error bars represent standard deviations. **b**, The shape of the  $e_g$  electron points directly towards the surface O atom and plays an important role during  $\text{O}_2^{2-}/\text{OH}^-$  exchange. O, B and H atoms are coloured red, blue and green, respectively.

molecule overlaps the  $\text{O}-2p_\sigma$  orbital more strongly than the overlap between the  $t_{2g}$  and  $\text{O}-2p_\pi$  orbitals, suggesting that the filling of  $e_g$  rather than  $t_{2g}$  of the B-ion should more accurately determine both the energy gained by adsorption/desorption of oxygen on B ions and the ORR activity if such an adsorption/desorption process was involved in the rate-limiting step of the ORR. This conjecture is supported by the correlation between increasing  $e_g$  filling and decreasing onset temperature for oxygen release (measured by  $\text{O}_2$  temperature-programmed desorption), in the order  $\text{LaCrO}_3$  ( $e_g = 0$ )  $>$   $\text{LaMnO}_3$  ( $e_g = 1$ )  $\approx$   $\text{LaCoO}_3$  ( $e_g \approx 1$ )  $\approx$   $\text{LaNiO}_3$  ( $e_g \approx 1$ )  $>$   $\text{LaFeO}_3$  ( $e_g = 2$ )<sup>29</sup>, which is indicative of the strength of bonding between B-site cations and oxygen. We have taken into account whether partial substitution on the A or B sites features charge compensation via oxygen vacancy or changing of the B-ion valency in the  $e_g$  calculation of surface B ions, determined from a combination of literature data, thermogravimetry and XAS (Supplementary Figs S3, S4 and Table S1). Plotting ORR activity as a function of  $e_g$ -filling produces a definitive volcano plot (Fig. 2a) with a voltage span of  $0.25$  V, which corresponds to a change of  $\sim 4$  orders of magnitude in intrinsic ORR activity (using an  $\sim 60$  mV/decade Tafel slope.)

### Proposed ORR mechanism

We explain the volcano trend in the oxide ORR activity as follows. Too little  $e_g$ -filling in  $\text{La}_{1-x}\text{Ca}_x\text{CrO}_3$  ( $t_{2g}^3e_g^0$  for  $x = 0$ ,  $t_{2g}^{2.5}e_g^0$  for  $x = 0.5$ ) can result in B– $\text{O}_2$  bonding that is too strong, whereas too

much  $e_g$ -filling in  $\text{La}_{1-x}\text{Ca}_x\text{FeO}_3$  ( $t_{2g}^3e_g^2$  for  $x = 0$ ,  $t_{2g}^3e_g^{1.75}$  for  $x = 0.25$ ,  $t_{2g}^3e_g^{1.5}$  for  $x = 0.5$ ) and  $\text{La}_{1+x}\text{NiO}_{3+x}$  [ $(\text{LaNiO}_3)_{1-x}(\text{La}_2\text{NiO}_4)_x$ , with  $(1-x)t_{2g}^3e_g^1 + xt_{2g}^3e_g^2$ ] can lead to an  $\text{O}_2$  interaction that is too weak; neither situation is optimum for ORR activity. On the other hand, a moderate amount of  $e_g$ -filling ( $\sim 1$ ) in  $\text{La}_{1-x}\text{Ca}_x\text{MnO}_3$  ( $t_{2g}^3e_g^1$  for  $x = 0$ ,  $t_{2g}^3e_g^{0.5}$  for  $x = 0.5$ ),  $\text{LaCoO}_3$  ( $t_{2g}^3e_g^1$ ) and  $\text{LaNiO}_3$  ( $t_{2g}^3e_g^1$ ) yields the highest activity. The striking correlation between  $e_g$ -filling and four orders of magnitude of ORR activity suggests that the  $e_g$ -filling represents a unifying and primary descriptor for the ORR activity of these oxides. The importance of  $e_g$ -filling also explains the origin of the peaks at high-spin  $d^4$  and low-spin  $d^7$  in the M plot of ORR activity versus the number of  $d$  electrons (Fig. 1d): both have  $e_g$ -filling  $\approx 1$ . The M shape thus arises from the spin-state transition on the B ions from high spin ( $d < 6$ ) to low spin ( $d > 6$ ).

The importance of a single  $e_g$  electron for ORR catalysis can be molecularly explained by the previous proposal that competition between the  $\text{O}_2^{2-}/\text{OH}^-$  displacement (Step 1) and  $\text{OH}^-$  regeneration (Step 4) on the surface of transition-metal ions is rate-limiting for ORR in an alkaline solution<sup>30</sup> (Fig. 3). In this scheme, B is a transition-metal cation with an  $e_g$  electron ordered into an orbital directed towards the surface  $\text{OH}^-$  ion. As a first order of approximation, the kinetics of the  $\text{O}_2^{2-}/\text{OH}^-$  exchange can be rationalized in terms of the energy gained by breaking the B– $\text{OH}^-$  bond to form B– $\text{O}_2^{2-}$ . The presence of a single  $e_g$  (Supplementary Scheme S2) represents a  $\sigma^*$  electron that can serve to destabilize the B– $\text{OH}^-$  bond and promote the  $\text{O}_2^{2-}/\text{OH}^-$  exchange reaction. The displacement of the  $\text{OH}^-$  ion that encounters a  $\sigma^*$  electron in the B– $\text{OH}^-$  bond by the  $\text{O}_2 + e^-$  (or  $\text{O}_{2,\text{ads}}^-$ ) species removes the highly energetic  $\sigma^*$  electron from the B– $\text{OH}^-$  bond to give a more stable B– $\text{O}_2^-$  configuration. If the  $e_g$  electron filling is more than 1 (the right branch in Fig. 2a), the  $\text{O}_2^{2-}/\text{OH}^-$  exchange does not gain sufficient energy during the displacement and the ORR kinetics can be limited by the rate of the  $\text{O}_2/\text{OH}^-$  exchange (Step 1). In contrast, if there is less than one  $e_g$  electron on the B cation (the left branch in Fig. 2a), the B– $\text{O}_2$  is not sufficiently destabilized and the ORR kinetics can instead be limited by the rate of surface  $\text{OH}^-$  regeneration (Step 4).

Although our observation of the importance of  $\sigma^*$ -electron transfer to  $\text{O}_2$  in ORR activity is in qualitative agreement with the previous hypothesis of Matsumoto *et al.*<sup>18–20</sup>, our work offers a quantitative correlation between the  $e_g$ -filling of surface transition-metal ions and intrinsic ORR activity of up to four orders of magnitude, and predicts  $e_g \approx 1$  to be key for developing the highest activity. In addition, an important distinction of our analysis is the assumption of a localized  $e_g$  electron in an orbital directed towards an  $\text{O}_2$  molecule from the surface B cations instead of

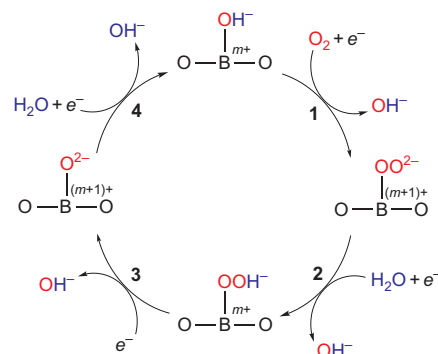


**Figure 3 | Proposed ORR mechanism on perovskite oxide catalysts<sup>30</sup>.** The ORR proceeds via four steps: 1, surface hydroxide displacement; 2, surface peroxide formation; 3, surface oxide formation; 4, surface hydroxide regeneration.

traditional band theory<sup>18–20</sup>. In the following text, we discuss many works that have provided evidence in support of this assumption. In the case of  $\text{LaNiO}_3$ , which has itinerant bulk  $\sigma^*$  electrons, the site symmetry of the bulk rhombohedral structure in  $\text{LaNiO}_3$  does not permit localization of an  $e_g$  electron in the bulk; however, the symmetry of a surface B site becomes tetragonal, which allows ordering of a localized  $e_g$  electron so as to be directed towards the surface anion species. This phenomenon is also demonstrated in low-temperature  $\text{LaCoO}_3$ , where  $e_g$  localization gives rise to the ferromagnetic surface intermediate-spin  $\text{Co(III)}:t_{2g}^5e_g^1$ , despite the low-spin  $\text{Co(III)}:t_{2g}^6e_g^0$  bulk phase<sup>24</sup>. A similar argument applies to the metallic system  $\text{La}_{1-x}\text{Sr}_x\text{MnO}_3$ , which exhibits a transition with increasing  $x$  from localized  $e_g$  electrons to a narrow  $\sigma^*$  band on the high-spin Mn atoms in the bulk<sup>23</sup>. Here, localization of the surface  $e_g$  electrons is stabilized by a reduction in the number of Mn near-neighbours as well as by site symmetry.

### B–O covalency on ORR activity

To further support that the  $e_g$ -filling of surface B ions governs ORR activity, we examined the influence of the covalency of the B–O bond of the perovskites on the ORR activity. A stronger covalency of the B–O bond should increase the driving force and thereby facilitate the  $\text{O}_2^-/\text{OH}^-$  exchange on the surface B ions, which can be considered as the rate-limiting step of ORR for oxides (Fig. 3). To quantify the B–O bond covalency of the perovskites, we performed O K-edge XAS, which revealed excitations from the O 1s orbital to unoccupied states above the Fermi level from regions within  $\sim 10$  nm of the surface (50% of the signal comes from the top 1 nm; ref. 31). The O K-edge spectra collected from selected perovskites (Fig. 4a) consist of two major excitations: O 1s  $\rightarrow$  B 3d – O 2p bands from 527 to 533 eV, and O 1s  $\rightarrow$  La 5d – O 2p bands from 533 to 537 eV (ref. 32). The specificity of the 1s  $\rightarrow$  2p excitation in the former permits quantification of the covalency or hybridization ( $\beta^2$ ) effect of the perovskites in this study (see Supplementary Methods). We found that the hybridization generally affects the ORR activity positively (Supplementary Fig. S5). To probe the effect of hybridization on the ORR activity without interference from the  $e_g$ -filling effect, we plotted the influence of the hybridization parameter on the ORR activity of perovskites at constant  $e_g$ -filling in Fig. 4b. Increasing hybridization positively affects ORR activity (Fig. 4b), which is in agreement with the molecular picture of the proposed ORR mechanism.

### Conclusions

This work shows that the design principle for enhancing the ORR activity of transition-metal-oxide perovskites is an  $e_g$ -filling having a value of  $\sim 1$  for maximum activity, which can be further improved by increasing the covalency between the metal 3d and oxygen 2p orbitals. Our findings can be explained by competition between a rate-limiting  $\text{O}_2^{2-}/\text{OH}^-$  exchange (Step 1 in Fig. 3) and the regeneration of  $\text{OH}^-$  on the surface (Step 4 in Fig. 3). This exchange depends on the energy gained by transferring a single  $\sigma^*$ -antibonding  $e_g$  electron of the B–OH $^-$  bond to the  $\text{O}_2^{2-}$  adsorbates, thereby stabilizing the displacement. The greater the covalent contribution to the B– $\text{O}_2^{2-}$  bond, the greater the energy realized by the exchange to stabilize the adsorbate, and therefore the faster ORR kinetics. This work shows that tuning surface electronic structure features such as transition-metal  $e_g$ -filling and covalency is a promising strategy in developing highly active non-precious-metal-containing oxide catalysts for oxygen reduction in electrochemical conversion and storage devices. Considering the synergism between the OER and the ORR expected from the pioneering *ab initio* works of Rossmeisl *et al.*<sup>33</sup>, these descriptors could also influence the OER activity of oxides, and such a study would test the validity of the proposed influence of  $e_g$ -filling of transition-metal ions on  $\text{O}_2$  electrocatalysis.

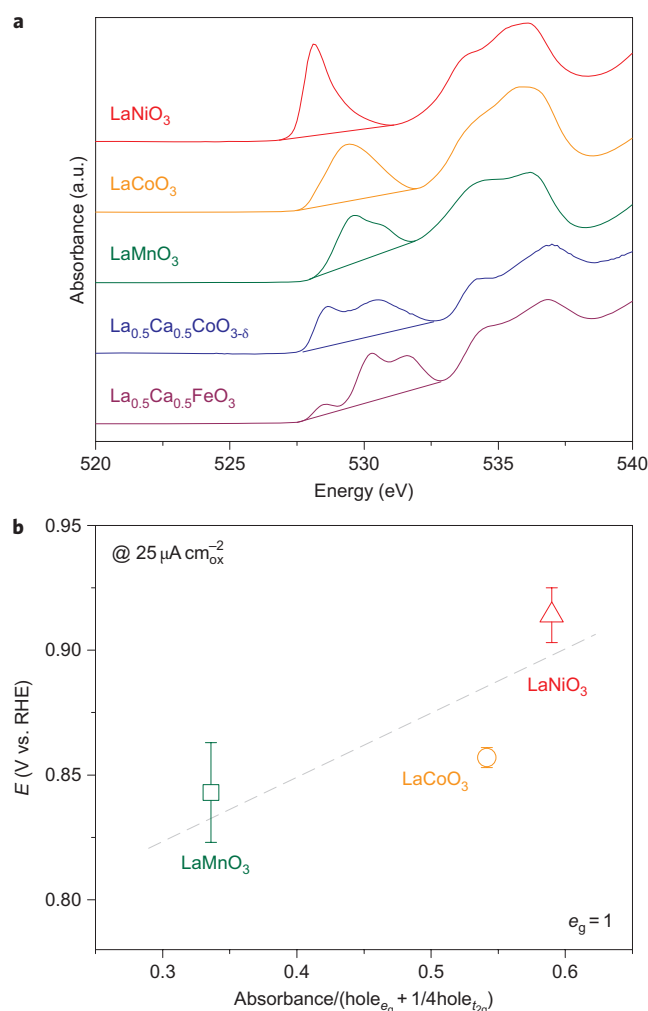


**Figure 4 | Role of B–O covalency on the ORR activity of perovskite oxides.**

**a**, O K-edge XAS of  $\text{La}_{0.5}\text{Ca}_{0.5}\text{FeO}_3$ ,  $\text{La}_{0.5}\text{Ca}_{0.5}\text{CoO}_{3-\delta}$ ,  $\text{LaMnO}_3$ ,  $\text{LaCoO}_3$  and  $\text{LaNiO}_3$ . Pre-edge bands, corresponding to the transition to the Me 3d and O 2p unoccupied bands, are shown with linear backgrounds. **b**, Potentials at  $25 \mu\text{A cm}^{-2}$  as a function of the B–O covalency, which is estimated by the normalized absorbance (see Supplementary Methods) at  $e_g$ -filling = 1. Error bars represent standard deviations of at least three measurements.

### Methods

**Material synthesis.** The perovskites samples used in this study were synthesized using a co-precipitation method. Rare and alkaline earth nitrate and transition-metal nitrate (both 99.98%, Alfa Aesar) in a 1:1 mole ratio were mixed in Milli-Q water (18 MΩ cm) at a metal concentration of 0.2 M. The solution containing rare and alkaline earth and transition metals was titrated with 1.2 M tetramethylammonium hydroxide (100% Alfa Aesar). The precipitate was filtered, collected and dried. The powder samples were subjected to heat treatment at  $1,000^\circ\text{C}$  under an Ar atmosphere for the  $\text{La}_{1-x}\text{Ca}_x\text{MnO}_3$  ( $x = 0, 0.5$ ) and  $\text{La}_{0.5}\text{Ca}_{0.5}\text{CrO}_3$ ,  $\text{LaNi}_{0.5}\text{Mn}_{0.5}\text{O}_3$  and  $\text{LaCu}_{0.5}\text{Mn}_{0.5}\text{O}_3$  samples, at  $1,000^\circ\text{C}$  under a dry air atmosphere for  $\text{LaCrO}_3$ ,  $\text{La}_{1-x}\text{Ca}_x\text{FeO}_3$  ( $x = 0, 0.25, 0.5$ ),  $\text{La}_{1-x}\text{Ca}_x\text{CoO}_3$  ( $x = 0, 0.5$ ),  $\text{La}_3\text{Ni}_2\text{O}_7$  and  $\text{La}_4\text{Ni}_3\text{O}_{10}$  samples, and at  $800^\circ\text{C}$  under an  $\text{O}_2$  atmosphere for the  $\text{LaNiO}_3$  sample.  $\text{LaMnO}_{3+\delta}$  was prepared from an  $800^\circ\text{C}$  heat treatment of  $\text{LaMnO}_3$  in air.  $\text{La}_2\text{NiO}_4$  was synthesized in two steps: heated at  $1,000^\circ\text{C}$  under an air atmosphere and then at  $800^\circ\text{C}$  under an Ar atmosphere. All gases were ultrahigh-grade purity (Airgas). All samples were characterized by X-ray diffraction to determine phase purity with a Rigaku high-power rotating anode X-ray powder diffractometer at a scan rate of  $0.8^\circ \text{min}^{-1}$ . All X-ray diffraction data and refined lattice parameters are shown in Supplementary Table S2. All oxides used in this study had a single phase except  $\text{LaNiO}_3$ , where  $<2\%$  of NiO was present. Average particle sizes with standard deviations and estimated surface area values were quantified using a Philips XL30 FEG ESEM (FEI-Philips) and are listed in Supplementary Table S3.

**Electrode preparation.** Glassy-carbon electrodes (diameter, 5 mm; Pine Instrument) were polished with  $0.05 \mu\text{m}$  alumina slurry (Buehler) to obtain a mirror



finish. Perovskite oxides were mixed with acid-treated acetylene black (Chevron) at a mass ratio of 5:1. Catalyst ink was prepared by mixing perovskite oxides and acetylene black with tetrahydrofuran (99.9 + % Sigma-Aldrich) and an appropriate amount of neutralized Nafion (5% weight, Ion power) as described elsewhere<sup>15</sup>. The electrode had a final composition of 250  $\mu\text{g}_{\text{oxide}} \text{cm}^{-2}_{\text{disk}}$ , 50  $\mu\text{g}_{\text{AB}} \text{cm}^{-2}_{\text{disk}}$  and 50  $\mu\text{g}_{\text{Nafion}} \text{cm}^{-2}_{\text{disk}}$ .

**Electrochemical characterization.** Electrochemical measurements were conducted with a rotating-disk electrode (Pine Instrument). All measurements were collected in a 100 ml solution of 0.1 M KOH, prepared from Milli-Q water (18 M $\Omega$  cm) and KOH pellets (99.99% weight, Sigma-Aldrich), with a VoltaLab PST050 potentiostat. In this work, error bars represent standard deviations from at least three independent repeat measurements. Analysis of ORR kinetic currents has been described in our previous work<sup>15</sup>, and specific ORR activity was obtained by normalizing the kinetic current with the surface area of each oxide estimated from scanning electron microscopy (SEM) images (Supplementary Table S3). Because the errors associated with the estimation of surface area (Supplementary Table S3) were smaller than experimental uncertainty in the intrinsic ORR activity of oxides from our rotating disk electrode (RDE) measurements ( $\sim 30$  mV standard deviation in Fig. 2a, translating to a change by a factor of  $\sim 3.2$  in ORR current density normalized to the oxide surface when considering a Tafel slope of 60 mV/decade), the ORR trend and values presented in Fig. 2 were not affected significantly by errors in the oxide surface area. In addition, Brunauer–Emmett–Teller (BET) measurements of the surface areas of selected oxides showed reasonable agreement with those estimated from the SEM images (for example,  $\text{LaNiO}_3$ , 5.6 m $^2 \text{g}^{-1}$  from BET measurements versus 3.5 m $^2 \text{g}^{-1}$  estimated from SEM images). Moreover, it should be noted that the specific ORR current densities for  $\text{LaCrO}_3$  and  $\text{LaFeO}_3$  were comparable to the ORR activity of acetylene black (background ORR activity), taking into account experimental uncertainty<sup>15</sup>, so the ORR activity values reported here can only be regarded as upper limits for these two oxides. Furthermore, the ORR activity results obtained from thin-film RDE measurements can be well translated to the actual performance of an air electrode in fuel cells and metal–air batteries, as shown previously for PEMFCs<sup>34</sup>. Finally, preliminary stability testing of the most active oxide,  $\text{LaMnO}_{3+\delta}$ , revealed only very small changes in ORR activity (smaller than the experimental uncertainty in the RDE measurements shown in Fig. 2a) over 3.5 h of continuous cycling between 0.7 and 1.0 V versus RHE, suggesting that oxide materials can serve as reasonably stable ORR catalysts in fuel cells and metal–air batteries.

Received 22 March 2011; accepted 11 May 2011;  
published online 12 June 2011; corrected online 17 June 2011

## References

- Gasteiger, H. A. & Markovic, N. M. Just a dream-or future reality? *Science* **324**, 48–49 (2009).
- Whitesides, G. M. & Crabtree, G. W. Don't forget long-term fundamental research in energy. *Science* **315**, 796–798 (2007).
- Gray, H. B. Powering the planet with solar fuel. *Nature Chem.* **1**, 7 (2009).
- Lewis, N. S. & Nocera, D. G. Powering the planet: chemical challenges in solar energy utilization. *Proc. Natl Acad. Sci. USA* **103**, 15729–15735 (2006).
- Kanan, M. W. & Nocera, D. G. *In situ* formation of an oxygen-evolving catalyst in neutral water containing phosphate and  $\text{Co}^{2+}$ . *Science* **321**, 1072–1075 (2008).
- Service, R. F. Transportation research hydrogen cars: fad or the future? *Science* **324**, 1257–1259 (2009).
- Armand, M. & Tarascon, J. M. Building better batteries. *Nature* **451**, 652–657 (2008).
- Lu, Y. C. *et al.* Platinum–gold nanoparticles: a highly active bifunctional electrocatalyst for rechargeable lithium–air batteries. *J. Am. Chem. Soc.* **132**, 12170–12171 (2010).
- Norskov, J. K. *et al.* Origin of the overpotential for oxygen reduction at a fuel-cell cathode. *J. Phys. Chem. B* **108**, 17886–17892 (2004).
- Stamenkovic, V. R. *et al.* Improved oxygen reduction activity on  $\text{Pt}_3\text{Ni}(111)$  via increased surface site availability. *Science* **315**, 493–497 (2007).
- Stamenkovic, V. R. *et al.* Changing the activity of electrocatalysts for oxygen reduction by tuning the surface electronic structure. *Angew. Chem. Int. Ed.* **45**, 2897–2901 (2006).
- Lima, F. H. B. *et al.* Catalytic activity *d*-band center correlation for the  $\text{O}_2$  reduction reaction on platinum in alkaline solutions. *J. Phys. Chem. C* **111**, 404–410 (2007).
- Greeley, J. *et al.* Alloys of platinum and early transition metals as oxygen reduction electrocatalysts. *Nature Chem.* **1**, 552–556 (2009).
- Meadowcroft, D. B. Low-cost oxygen electrode material. *Nature* **226**, 847–848 (1970).
- Suntivich, J., Gasteiger, H. A., Yabuuchi, N. & Shao-horn, Y. Electrocatalytic measurement methodology of oxide catalysts using a thin-film rotating disk electrode. *J. Electrochem. Soc.* **157**, B1263–B1268 (2010).
- Bockris, J. O. & Otagawa, T. The electrocatalysis of oxygen evolution on perovskites. *J. Electrochem. Soc.* **131**, 290–302 (1984).
- Zou, Z. G., Ye, J. H., Sayama, K. & Arakawa, H. Direct splitting of water under visible light irradiation with an oxide semiconductor photocatalyst. *Nature* **414**, 625–627 (2001).
- Matsumoto, Y., Yoneyama, H. & Tamura, H. Influence of nature of conduction-band of transition-metal oxides on catalytic activity for oxygen reduction. *J. Electroanal. Chem.* **83**, 237–243 (1977).
- Matsumoto, Y., Yoneyama, H. & Tamura, H. Catalytic activity for electrochemical reduction of oxygen of lanthanum nickel-oxide and related oxides. *J. Electroanal. Chem.* **79**, 319–326 (1977).
- Matsumoto, Y., Yoneyama, H. & Tamura, H. A new catalyst for cathodic reduction of oxygen: lanthanum nickel oxide. *Chem. Lett.* 661–662 (1975).
- Bockris, J. O. & Otagawa, T. Mechanism of oxygen evolution on perovskites. *J. Phys. Chem.* **87**, 2960–2971 (1983).
- Morin, F. J. & Wolfram, T. Surface states and catalysis on *d*-band perovskites. *Phys. Rev. Lett.* **30**, 1214–1217 (1973).
- Goodenough, J. B. & Zhou, J. S. in *Localized to Itinerant Electronic Transition in Perovskite Oxides* Vol. 98, 17–113 (Springer-Verlag Berlin, 2001).
- Yan, J. Q., Zhou, J. S. & Goodenough, J. B. Ferromagnetism in  $\text{LaCoO}_3$ . *Phys. Rev. B* **70**, 014402 (2004).
- Markovic, N. M., Gasteiger, H. A. & Ross, P. N. Oxygen reduction on platinum low-index single-crystal surfaces in alkaline solution: rotating ring disk (Pt(*hkl*)) studies. *J. Phys. Chem.* **100**, 6715–6721 (1996).
- Fernandez, E. M. *et al.* Scaling relationships for adsorption energies on transition metal oxide, sulfide, and nitride surfaces. *Angew. Chem. Int. Ed.* **47**, 4683–4686 (2008).
- Tejuka, L. G., Fierro, J. L. G. & Tascon, J. M. D. Structure and reactivity of perovskite-type oxides. *Adv. Catal.* **36**, 237–328 (1989).
- Dowden, D. A. Crystal and ligand field models of solid catalysts. *Catal. Rev.* **5**, 1–32 (1971).
- Yokoi, Y. & Uchida, H. Catalytic activity of perovskite-type oxide catalysts for direct decomposition of NO: correlation between cluster model calculations and temperature-programmed desorption experiments. *Catal. Today* **42**, 167–174 (1998).
- Goodenough, J. B. & Cushing, B. L., in *Handbook of Fuel Cells — Fundamentals, Technology and Applications* Vol. 2, 520–533 (eds Vielstich, W., Gasteiger, H. A. & Yokokawa, H. (Wiley, 2003)).
- Abbate, M. *et al.* Probing depth of surface X-ray absorption spectroscopy measured in total electron-yield-mode. *Surf. Interface Anal.* **18**, 65–69 (1992).
- Abbate, M. *et al.* Controlled-valence properties of  $\text{La}_{1-x}\text{Sr}_x\text{FeO}_3$  and  $\text{La}_{1-x}\text{Sr}_x\text{MnO}_3$  studied by soft-X-ray absorption-spectroscopy. *Phys. Rev. B* **46**, 4511–4519 (1992).
- Rossmeisl, J., Qu, Z. W., Zhu, H., Kroes, G. J. & Norskov, J. K. Electrolysis of water on oxide surfaces. *J. Electroanal. Chem.* **607**, 83–89 (2007).
- Gasteiger, H. A., Kocha, S. S., Sompalli, B. & Wagner, F. T. Activity benchmarks and requirements for Pt, Pt-alloy, and non-Pt oxygen reduction catalysts for PEMFCs. *Appl. Catal. B* **56**, 9–35 (2005).

## Acknowledgements

This work was supported by Toyota Motor Company and by the DOE Hydrogen Initiative programme (award no. DE-FG02-05ER15728). The research made use of the Shared Experimental Facilities supported by the MRSEC Program of the National Science Foundation (award no. DMR 08-019762). J.S. was supported in part by the Chesonis Foundation Fellowship. J.B.G. was supported by the Robert A. Welch Foundation (Houston, Texas). The authors would like to thank A. Mansour for his help with X-ray absorption spectroscopy. The National Synchrotron Light Source is supported by the US Department of Energy, Division of Material Sciences and Division of Chemical Sciences (contract no. DE-AC02-98CH10886). The beamline X11 is supported by the Office of Naval Research and contributions from Participating Research Team (PRT) members.

## Author contributions

Y.S.H. proposed the concept. J.S., H.A.G. and Y.S.H. designed the experiments. J.S., N.Y. and H.N. carried out the experiments. J.S., H.A.G., J.B.G. and Y.S.H. performed the analysis and wrote the manuscript.

## Additional information

The authors declare no competing financial interests. Supplementary information accompanies this paper at [www.nature.com/naturechemistry](http://www.nature.com/naturechemistry). Reprints and permission information is available online at <http://www.nature.com/reprints/>. Correspondence and requests for materials should be addressed to H.A.G. and Y.S.H.

## Design Principles for Oxygen Reduction Activity on Perovskite Oxide Catalysts for Fuel Cells and Metal-Air Batteries

Jin Suntivich<sup>1,†</sup>, Hubert A. Gasteiger<sup>2,†,§</sup>, Naoaki Yabuuchi<sup>2,†</sup>,  
Haruyuki Nakanishi<sup>3</sup>, John B. Goodenough<sup>4</sup>, Yang Shao-Horn<sup>\*,1,2,†</sup>

<sup>1</sup> *Materials Science and Engineering Department,*

<sup>2</sup> *Mechanical Engineering Department,*

<sup>†</sup> *Electrochemical Energy Laboratory,*

*Massachusetts Institute of Technology, 31-056,*

*77 Massachusetts Ave, Cambridge, MA 02139, USA*

<sup>3</sup> *Fuel Cell System Development Division, Toyota Motor Corporation*

*Higashifuji Technical Center 1200, Mishuku, Susono, Shizuoka 410-1193, Japan*

<sup>4</sup> *Texas Materials Institute, University of Texas at Austin,*

*ETC 9.184, Austin, TX 78712, USA*

<sup>§</sup> *Present Address: Department of Chemistry, Technische Universität München,*

*Lichtenbergstrasse 4, D-85747 Garching, Germany*

\* E-mail: [shaohorn@mit.edu](mailto:shaohorn@mit.edu)

Index	Page
Supplementary methods	2-6
Table S1-S3	7-9
Scheme S1-S2	10-11
Figure S1-S5	12-17
Reference	18-19

## Supplementary methods

*Soft X-ray Absorption characterization.* O K-edge XAS was collected at Saga Synchrotron (BL12), Japan. All measurements were collected in electron-yield mode at  $10^{-7}$  Pa pressure. All spectra were normalized to the O atomic absorption at  $\sim 550$  eV. In a band corresponding to the O  $1s$  to B  $3d$  - O  $2p$  excitation, the spectra probe the  $u$  symmetry portion of the unoccupied state, but not the  $g$  symmetry portion as the latter is forbidden by the selection rule. In a pseudocubic approximation of the perovskite structure, the  $u$  symmetry portion is intrinsic to the  $2p$  orbital of the O atom and the absorbance is related to the unoccupied  $2p$  orbital (“ligand hole”). The amount of the hybridization is defined by the intensity of the ligand-hole normalized to the density of the B  $3d$  - O  $2p$  unoccupied state, viz., the ligand character of each B  $3d$  - O  $2p$  hole. To account for the difference in the ligand-hole strength between the  $e_g$  symmetry and the  $t_{2g}$  symmetry, an appropriate prefactor assuming 2x reduction in  $t_{2g}$  transfer integral in comparison to  $e_g$  (which corresponds to 4x reduction in ligand-hole strength) is applied<sup>1</sup>. Applying the dipole operator approximation, the hybridization of B and O atoms in an octahedral environment can be quantified by the following parameter:

$$|\beta|^2 \propto \frac{\text{Absorbance}}{\text{hole}_{E_g} + \frac{1}{4}\text{hole}_{T_{2g}}}$$

In this definition, absorbance is the integrated area of the O  $1s \rightarrow$  B  $3d$  - O  $2p$  band in the O K-edge minus the fitted linear background (see Figure 4a)<sup>2</sup>, and the holes (unoccupied states) for  $e_g$  and  $t_{2g}$  are defined by the unoccupied density of states of  $e_g$  and  $t_{2g}$  orbitals respectively (see Table S1 for values). The  $\frac{1}{4}$  prefactor of the  $t_{2g}$  hole accounts for the difference in transfer integral between  $t_{2g}$  and  $e_g$ .

*Hard X-ray Absorption characterization.* Hard XAS was collected at beamline X11A of the National Synchrotron Light Source at the Brookhaven National Laboratory with the electron storage ring of 2.8 GeV and a current in the range of 150–300 mA. The Mn, Ni, Co, and Fe K-edge electron yield modes were collected from oxide powders mounted on carbon conductive tape with a Lytle detector at room temperature using Si(111) double-crystal monochromator detuned to ~70% of the maximum intensity. The spectra were calibrated to the reference metal foils by setting the maximum inflection points ( $E_0$ ) to their respective reference energies. X-ray absorption near edge structure (XANES) was extracted from the absorbance with the IFEFFIT package by subtracting from the pre-edge region with a linear fit and normalizing to a per atomic basis with the average of the absorption cross section over the post-edge region<sup>3</sup>.

*Determination of  $e_g$  filling of non-stoichiometric  $\text{LaMnO}_{3+\delta}$ .* Based on the published thermodynamics, subjecting  $\text{LaMnO}_3$  to a heat treatment in air at 800°C will result in a phase transformation to an oxygen over-stoichiometric  $\text{LaMnO}_{3+\delta}$  compound with  $\delta \approx 0.11$  ( $\pm 0.05$ )<sup>4</sup>. To ensure that the synthesis of  $\text{LaMnO}_{3+\delta}$  was successful, XRD was collected to confirm the rhombohedral phase of  $\text{LaMnO}_{3+\delta}$  (Table S2). From the published  $\delta \approx 0.11$ ,  $\text{LaMnO}_{3+\delta}$  has a high spin  $t_{2g}^3 e_g^{0.79}$  configuration and  $e_g$  filling of  $0.79$  ( $\pm 0.05$ )  $\approx 0.8$ <sup>4</sup>.

*Determination of  $e_g$  filling of Ca-substituted  $\text{La}_{0.5}\text{Ca}_{0.5}\text{MnO}_3$ .* Previous studies using X-ray emission spectroscopy<sup>4</sup>, thermogravimetric analysis (TGA)<sup>6</sup>, X-ray absorption near-edge spectroscopy (XANES)<sup>5</sup>, and magnetic measurement<sup>6</sup> have shown that charge compensation following Ca-substitution in  $\text{LaMnO}_3$  occurs via  $\text{Mn}^{4+}$  formation. We, therefore, assume that our  $\text{La}_{0.5}\text{Ca}_{0.5}\text{MnO}_3$  compound charge-compensates by forming



$\text{Mn}^{4+}$ . As a result,  $\text{La}_{0.5}\text{Ca}_{0.5}\text{MnO}_3$  has an average Mn oxidation state of 3.5+ and therefore an electron configuration of  $t_{2g}^3 e_g^{0.5}$ . We had conducted Mn K-edge XANES to confirm that the Mn in  $\text{La}_{0.5}\text{Ca}_{0.5}\text{MnO}_3$  shifts to higher oxidation state in relative to  $\text{LaMnO}_3$  (Figure S3a).

*Determination of  $e_g$  filling of Ca-substituted  $\text{La}_{0.75}\text{Ca}_{0.25}\text{FeO}_3$  and  $\text{La}_{0.5}\text{Ca}_{0.5}\text{FeO}_3$ .* The charge compensation following Ca-substitution in  $\text{LaFeO}_3$  is assumed to occur via  $\text{Fe}^{4+}$  formation in high spin configuration. This is in agreement with the observation of  $\text{Fe}^{4+}$  formation in Ca-substituted  $\text{LaFeO}_3$  using Mossbauer spectroscopy<sup>9,10</sup>. Our own Fe K-edge XANES also confirms that the Fe oxidation shifts to higher oxidation state with increasing Ca content (Figure S3b).

*Determination of  $e_g$  filling of Ca-substituted  $\text{La}_{0.5}\text{Ca}_{0.5}\text{CoO}_{3-\delta}$ .* Because the exact spin-state of  $\text{La}_{0.5}\text{Ca}_{0.5}\text{CoO}_{3-\delta}$  has not been determined yet in the literature, partly due to the fact that the majority of Co remains 3+ despite the substitution of  $\text{La}^{3+}$  by  $\text{Ca}^{2+}$  ion<sup>11</sup>, we approximate the spin state of this compound as a mixture of  $\text{LaCoO}_3$  and  $\text{SrCoO}_{2.5}$ . Using a mixture of intermediate spin  $\text{LaCoO}_3$  ( $t_{2g}^5 e_g^1$ )<sup>7</sup> and high spin  $\text{SrCoO}_{2.5}$  ( $t_{2g}^4 e_g^2$ )<sup>8</sup>, we arrive at an approximation of  $e_g \approx 1.5$  for  $\text{La}_{0.5}\text{Ca}_{0.5}\text{CoO}_{3-\delta}$ . The concept of high-spin Co stabilization with Ca-substitution has been proposed in the literature<sup>11,14</sup>, so we believe our approximation is within reason, especially for the surface Co. We had also conducted TGA to confirm the formation of oxygen vacancy ( $\delta_{\text{TGA}} = 0.21 \pm 0.01$ ) that had been reported in the literature following Ca-substitution. Our Co K-edge XANES additionally demonstrated that the Co edge remained unchanged following Ca-substitution, which provides further evidence for the stabilization of  $\text{Co}^{3+}$  in  $\text{La}_{0.5}\text{Ca}_{0.5}\text{CoO}_{3-\delta}$  (Figure S3c).

*Determination of  $e_g$  filling of  $\text{LaNi}_{0.5}\text{Mn}_{0.5}\text{O}_3$  and  $\text{LaCu}_{0.5}\text{Mn}_{0.5}\text{O}_3$ .* The  $e_g$  filling for the mixed B-site compounds ( $\text{LaNi}_{0.5}\text{Mn}_{0.5}\text{O}_3$  and  $\text{LaCu}_{0.5}\text{Mn}_{0.5}\text{O}_3$ ) is complicated by the presence of two inequivalent B atoms and thus two different  $e_g$  fillings. In addition, it is widely known that a charge-ordered Mn/Ni undergoes charge-disproportionation into  $\text{Mn}^{4+}$  and  $\text{Ni}^{2+}$  in  $\text{LaNi}_x\text{Mn}_{1-x}\text{O}_3$ <sup>15</sup>. Thus, to determine properly the  $e_g$  filling for the mixed compounds, the oxidation state of both B atoms was measured with XANES. Using a known-relationship where  $E_0$  (maximum inflection point of the absorption edge) scales with oxidation state<sup>9</sup>, we estimate the valence state of Mn in both  $\text{LaNi}_{0.5}\text{Mn}_{0.5}\text{O}_3$  and  $\text{LaCu}_{0.5}\text{Mn}_{0.5}\text{O}_3$  to be 3.7 (high spin configuration, Figure S4a). A high-spin configuration of Mn leads to an  $e_g$  filling of 0.3 for the Mn site. Similar analysis was applied to Ni in  $\text{LaNi}_{0.5}\text{Mn}_{0.5}\text{O}_3$ , and the oxidation state of 2.3 was found (Figure S4b.) Based on this information, the  $e_g$  filling for Ni is thus determined to be 1.7 (low-spin configuration). While we did not perform this analysis on Cu in  $\text{LaCu}_{0.5}\text{Mn}_{0.5}\text{O}_3$ , we believe the Cu oxidation state should be close to that of Ni if not lower due to the higher electronegativity of Cu atom. Furthermore, the similarity in the Mn oxidation state between  $\text{LaNi}_{0.5}\text{Mn}_{0.5}\text{O}_3$  and  $\text{LaCu}_{0.5}\text{Mn}_{0.5}\text{O}_3$  also indicates that the Cu and the Ni oxidation state should be very close to each other ( $\approx 2.3+$ ). Thereby, we conclude that the  $e_g$  filling for Cu is 2.7 or higher. When we apply the  $e_g$  filling from either Mn or Ni (Cu) to the volcano plot, we have found that the use of  $e_g$  filling from Mn is most consistent with the observed activity trend (Figure 2a). Had we used the  $e_g$  filling of average B atoms, or Ni or Cu, the  $e_g$  would have resulted in an underestimation of the ORR activity. The consistency of selecting Mn  $e_g$  filling with our volcano plot also leads us to propose that the active site on the mixed compounds is the Mn atom, where both Ni and Cu atoms

had too many  $e_g$  electrons, rendering their catalytic properties inactive. The proposed Mn active site is consistent with our observation with the Ruddlesden-Popper compounds that Ni(+2) and Ni(+2.5) were not active for the ORR. Hence it is unlikely that Ni(2.3+), which was observed in  $\text{LaNi}_{0.5}\text{Mn}_{0.5}\text{O}_3$ , would be the active site.

**Table S1.** Summary of literature information on the spin state of the perovskite oxides

	Valence	Spin state	Assignment	Example of reference
<b>LaCrO<sub>3</sub></b>	Cr <sup>3+</sup>	n/a	$t_{2g}^3$	LS and HS identical
<b>LaMnO<sub>3</sub></b>	Mn <sup>3+</sup>	H.S.	$t_{2g}^3 e_g^1$	Magnetization <sup>6</sup>
<b>LaFeO<sub>3</sub></b>	Fe <sup>3+</sup>	H.S.	$t_{2g}^3 e_g^2$	Mossbäuer spectroscopy <sup>10</sup>
<b>LaCoO<sub>3</sub></b>	Co <sup>3+</sup>	I.S.	$t_{2g}^5 e_g^1$	Magnetization <sup>11</sup>
<b>LaNiO<sub>3</sub></b>	Ni <sup>3+</sup>	L.S.	$t_{2g}^6 e_g^1$	Extrapolation from RNiO <sub>3</sub> magnetization <sup>12,13</sup>
<b>La<sub>2</sub>NiO<sub>4</sub></b>	Ni <sup>2+</sup>	n/a	$t_{2g}^6 e_g^2$	LS and HS identical
<b>La<sub>4</sub>Ni<sub>3</sub>O<sub>10</sub></b>	Ni <sup>2.7+</sup>	L.S.	$t_{2g}^6 e_g^{1.3}$	Extrapolation from LaNiO <sub>3</sub> and La <sub>2</sub> NiO <sub>4</sub>
<b>LaNi<sub>0.5</sub>Mn<sub>0.5</sub>O<sub>3</sub></b>	Mn <sup>3.7+</sup> Ni <sup>2.3+</sup>	H.S. (Mn) L.S. (Ni)	$t_{2g}^3 e_g^{0.3}$ (Mn) $t_{2g}^6 e_g^{1.7}$ (Ni)	See Supplementary Method
<b>LaCu<sub>0.5</sub>Mn<sub>0.5</sub>O<sub>3</sub></b>	Mn <sup>3.7+</sup> Cu <sup>2.3+</sup>	H.S. (Mn) L.S. (Cu)	$t_{2g}^3 e_g^{0.3}$ (Mn) $t_{2g}^6 e_g^{2.7}$ (Cu)	See Supplementary Method
<b>La<sub>0.5</sub>Ca<sub>0.5</sub>CrO<sub>3-δ</sub></b> (Assume δ = 0)	Cr <sup>2.5+</sup>	n/a	$t_{2g}^{2.5}$	LS and HS identical
<b>La<sub>0.5</sub>Ca<sub>0.5</sub>MnO<sub>3-δ</sub></b> (Assume δ = 0)	Mn <sup>3.5+</sup>	H.S.	$t_{2g}^3 e_g^{0.5}$	Magnetization <sup>6</sup> , X-ray Emission <sup>4</sup>
<b>La<sub>0.5</sub>Ca<sub>0.5</sub>FeO<sub>3-δ</sub></b> (Assume δ = 0)	Fe <sup>3.5+</sup>	H.S.	$t_{2g}^3 e_g^{1.5}$	Mossbäuer spectroscopy <sup>9,10</sup>
<b>La<sub>0.75</sub>Ca<sub>0.25</sub>FeO<sub>3-δ</sub></b> (Assume δ = 0)	Fe <sup>3.25+</sup>	H.S.	$t_{2g}^3 e_g^{1.75}$	Mossbäuer spectroscopy <sup>9,10</sup>
<b>La<sub>0.5</sub>Ca<sub>0.5</sub>CoO<sub>3-δ</sub></b> (δ <sub>TGA</sub> = 0.21±0.01)	Co <sup>3+</sup>	I.S./H.S.	$t_{2g}^{4.5} e_g^{1.5}$	La <sub>1-x</sub> Ca <sub>x</sub> CoO <sub>3-δ</sub> extrapolation <sup>11</sup>
<b>LaMnO<sub>3+δ</sub></b> (Assume δ = 0.1)	Mn <sup>3.2+</sup>	H.S.	$t_{2g}^3 e_g^{0.8}$	X-ray Emission Spectroscopy <sup>4</sup>



**Table S2.** The derived lattice parameters of the oxide model compounds in this work

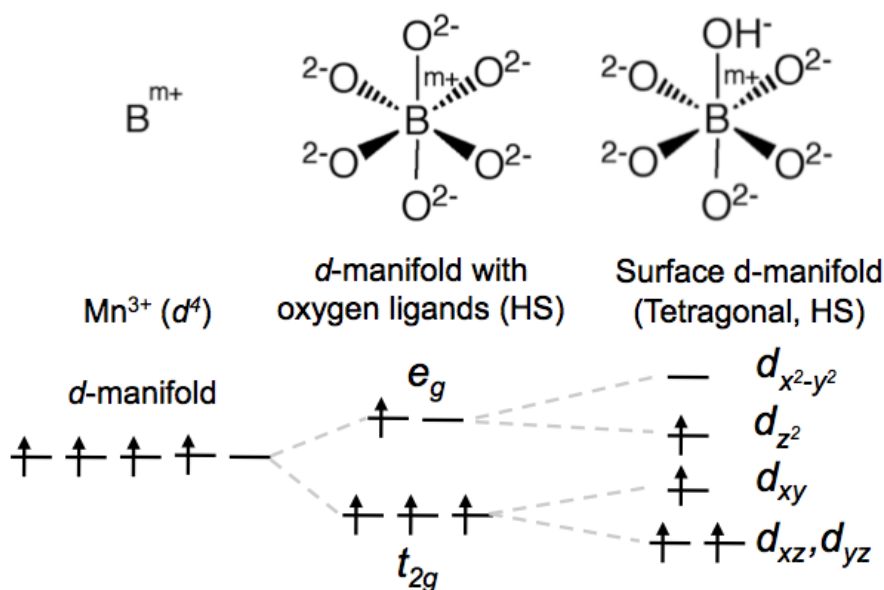
	Space group	a(Å)	b(Å)	c(Å)
<b>LaCrO<sub>3</sub></b>	P n m a	5.48	7.76	5.51
<b>LaMnO<sub>3</sub></b>	P n m a	5.66	7.72	5.53
<b>LaFeO<sub>3</sub></b>	P n m a	5.57	7.85	5.56
<b>LaCoO<sub>3</sub></b>	R -3 c	5.44	5.44	13.09
<b>LaNiO<sub>3</sub></b>	R -3 c	5.46	5.46	13.14
<b>La<sub>2</sub>NiO<sub>4</sub></b>	F m m m	5.47	5.46	12.68
<b>La<sub>4</sub>Ni<sub>3</sub>O<sub>10</sub></b>	F m m m	5.41	5.46	27.99
<b>LaNi<sub>0.5</sub>Mn<sub>0.5</sub>O<sub>3</sub></b>	P n m a	5.46	7.74	5.51
<b>LaCu<sub>0.5</sub>Mn<sub>0.5</sub>O<sub>3</sub></b>	P n m a	5.48	7.77	5.52
<b>La<sub>0.5</sub>Ca<sub>0.5</sub>CrO<sub>3-δ</sub></b>	P n m a	5.42	7.68	5.45
<b>La<sub>0.5</sub>Ca<sub>0.5</sub>MnO<sub>3-δ</sub></b>	P n m a	5.42	7.65	5.43
<b>La<sub>0.5</sub>Ca<sub>0.5</sub>FeO<sub>3-δ</sub></b>	P n m a	5.55	7.84	5.55
<b>La<sub>0.75</sub>Ca<sub>0.25</sub>FeO<sub>3-δ</sub></b>	P n m a	5.52	7.80	5.52
<b>La<sub>0.5</sub>Ca<sub>0.5</sub>CoO<sub>3-δ</sub></b>	P n m a	5.41	7.59	5.36
<b>LaMnO<sub>3+δ</sub></b>	R -3 c	5.52	5.52	13.35

**Table S3. Characterizations of the oxides studied in this work.**

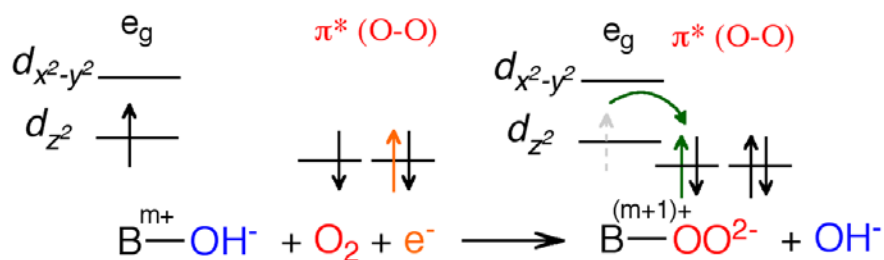
The number averaged diameter,  $d_{number}$ , the volume-area averaged diameter,  $d_{v/a}$ , and the specific surface area,  $A_s$ , were obtained from particle size distribution measurements.

Methodology for calculating each variable is given elsewhere<sup>14</sup>.

	$d_{number}$ ( $\mu\text{m}$ )	$d_{v/a}$ ( $\mu\text{m}$ )	$A_s$ ( $\text{m}^2 \text{g}^{-1}$ )
<b>LaCrO<sub>3</sub></b>	0.64 ( $\pm 0.25$ )	0.83	1.1
<b>LaMnO<sub>3</sub></b>	1.05 ( $\pm 0.52$ )	1.51	0.6
<b>LaFeO<sub>3</sub></b>	0.71 ( $\pm 0.34$ )	1.01	0.9
<b>LaCoO<sub>3</sub></b>	0.78 ( $\pm 0.40$ )	1.10	0.7
<b>LaNiO<sub>3</sub></b>	0.20 ( $\pm 0.06$ )	0.24	3.5
<b>La<sub>2</sub>NiO<sub>4</sub></b>	0.49 ( $\pm 0.25$ )	0.70	1.2
<b>La<sub>4</sub>Ni<sub>3</sub>O<sub>10</sub></b>	0.45 ( $\pm 0.15$ )	0.53	1.6
<b>LaNi<sub>0.5</sub>Mn<sub>0.5</sub>O<sub>3</sub></b>	0.34 ( $\pm 0.11$ )	0.81	1.1
<b>LaCu<sub>0.5</sub>Mn<sub>0.5</sub>O<sub>3</sub></b>	0.58 ( $\pm 0.28$ )	0.80	1.1
<b>La<sub>0.5</sub>Ca<sub>0.5</sub>CrO<sub>3-<math>\delta</math></sub></b>	0.19 ( $\pm 0.06$ )	0.22	4.9
<b>La<sub>0.5</sub>Ca<sub>0.5</sub>MnO<sub>3-<math>\delta</math></sub></b>	0.92 ( $\pm 0.44$ )	0.62	2.1
<b>La<sub>0.5</sub>Ca<sub>0.5</sub>FeO<sub>3-<math>\delta</math></sub></b>	0.62 ( $\pm 0.31$ )	0.89	1.1
<b>La<sub>0.75</sub>Ca<sub>0.25</sub>FeO<sub>3-<math>\delta</math></sub></b>	0.36 ( $\pm 0.22$ )	0.59	1.8
<b>La<sub>0.5</sub>Ca<sub>0.5</sub>CoO<sub>3-<math>\delta</math></sub></b>	0.43 ( $\pm 0.23$ )	0.63	1.6
<b>LaMnO<sub>3+<math>\delta</math></sub></b>	1.39 ( $\pm 0.58$ )	1.81	0.5



**Scheme S1. Molecular orbital of  $\text{BO}_6$  interaction.** The energy levels of the d-electrons in free B ion, octahedral  $\text{BO}_6$ , and surface  $\text{BO}_6$  configurations. The initial d manifold degeneracy is split into the antibonding  $e_g$  and  $t_{2g}$  levels.  $\text{Mn}^{3+} (d^4)$  in high spin configuration is shown as an example of a cation with an antibonding  $e_g$ -orbital degeneracy with a single  $e_g$  electron. At a surface cation, the degeneracy is removed by a tetragonal site symmetry in which the occupied  $e_g$  electron occupying a  $z^2$  orbital directed toward a surface  $\text{OH}^-$  is lowered in energy relative to the  $e_g$  electron occupying the  $x^2-y^2$  orbital.



**Scheme S2. The transfer of  $e_g$  electron during  $O_2^{2-}/OH^-$  displacement drives the reaction forward.** The rate-limiting step of the ORR is the surface hydroxide displacement. The kinetics of this step is determined by the driving force from the transfer of a  $\sigma^*$  electron to an O-O orbital.



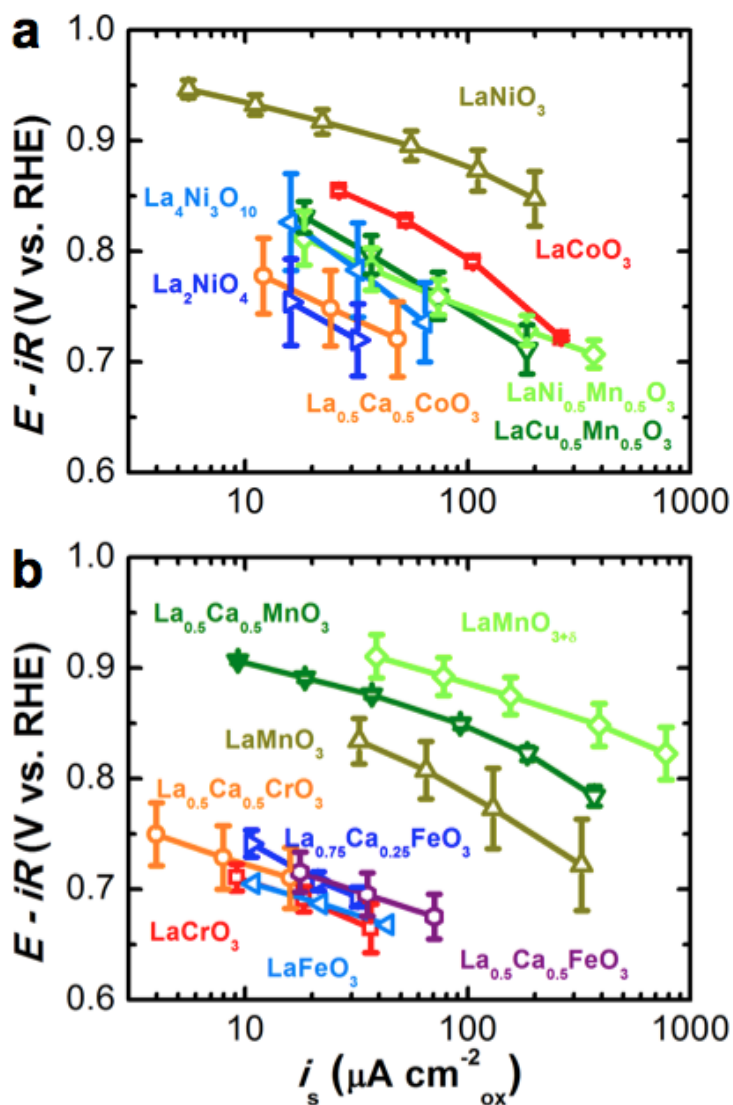


**Figure S1. (A-B) Tafel plot of the ORR specific activity of various oxides studied in this work using thin film RDE. All the activities are transport-compensated, iR-corrected, and normalized to the catalyst surface area.**

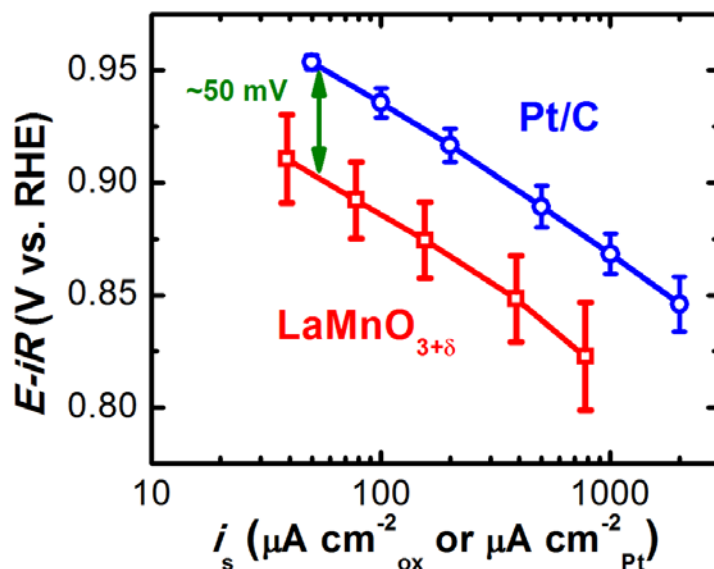


**Figure S2. Tafel plot of the ORR specific activity of LaMnO<sub>3+δ</sub> vs. Pt/C from the thin film RDE experiments.** These two catalysts have very similar ORR activities (~50 mV shift, corresponding to less than an order of activity difference). Error bars represent standard deviations of at least three independent measurements.

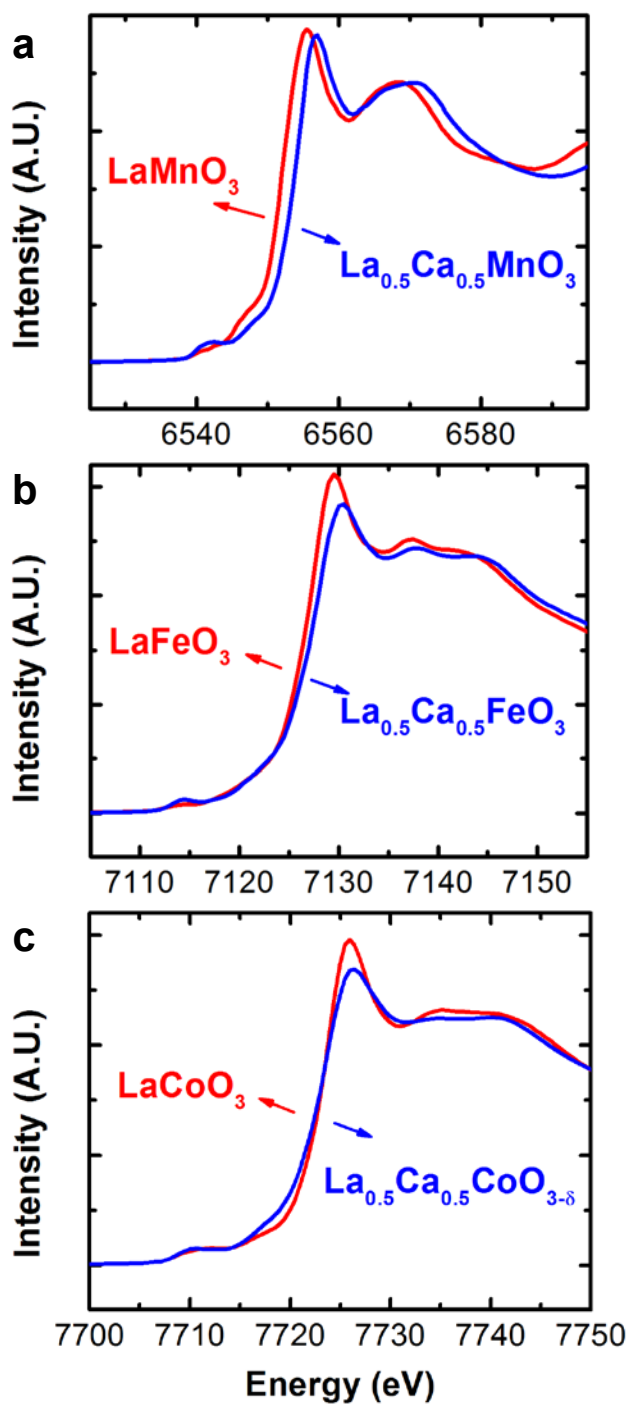


**Figure S3. XANES of LaBO<sub>3</sub> perovskite oxides vs. Ca-containing LaBO<sub>3</sub> (La<sub>0.5</sub>Ca<sub>0.5</sub>BO<sub>3</sub>). (a) B = Mn. The energy**

position of the  $\text{La}_{0.5}\text{Ca}_{0.5}\text{MnO}_3$  Mn K-edge is higher than that of  $\text{LaMnO}_3$ , which suggests that Mn in  $\text{La}_{0.5}\text{Ca}_{0.5}\text{MnO}_3$ , on average, has a higher oxidation state than  $\text{LaMnO}_3$ . (b) and (c) Similar analyses for B = Fe and Co respectively.



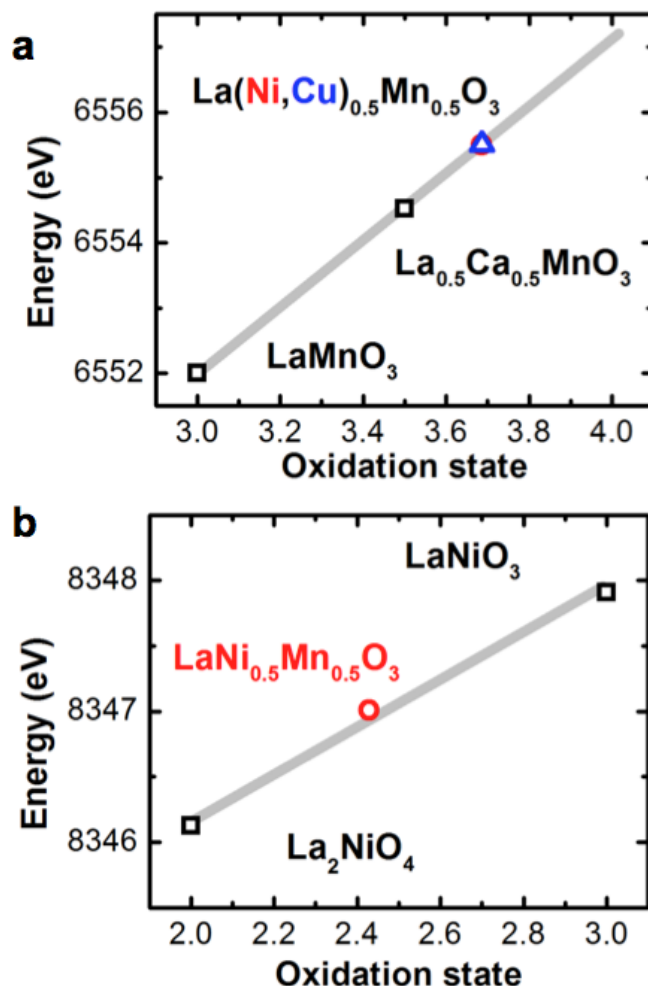


**Figure S4. Determination of oxidation state of Mn in  $\text{LaNi}_{0.5}\text{Mn}_{0.5}\text{O}_3$  and  $\text{LaCu}_{0.5}\text{Mn}_{0.5}\text{O}_3$  using XAS  $E_0$ 's relationship with the oxidation state.** (a) Mn oxidation state for both mixed compounds (● for  $\text{LaNi}_{0.5}\text{Mn}_{0.5}\text{O}_3$ , ▲ for  $\text{LaCu}_{0.5}\text{Mn}_{0.5}\text{O}_3$ ) is determined to be  $\approx 3.7+$ . (b) Similar analysis as (a) for Ni in  $\text{LaNi}_{0.5}\text{Mn}_{0.5}\text{O}_3$  (●). The oxidation state for Ni is determined to be  $\approx 2.3+$ .

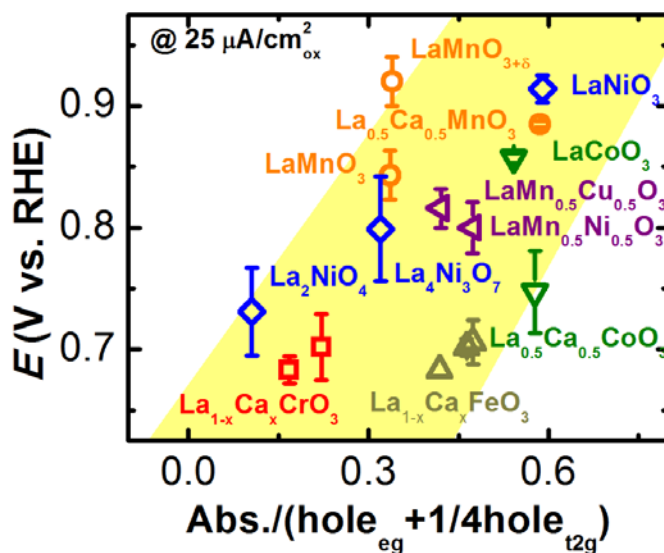


**Figure S5. The ORR benchmark potentials as a function of the normalized absorbance.** The weak dependence of the activity on the hybridization parameter is guided through a yellow band in the background. The data symbols vary with the type of B ions (■ for Cr, ● for Mn, ▲ for Fe, ▼ for Co, ◆ for Ni, and ▲ for mixed compounds), where  $x = 0$  and  $0.5$  for Cr, and  $0$ ,  $0.25$ , and  $0.5$  for Fe. Error bars represent standard deviations of at least three independent measurements.

## References

1. Medarde, M. et al., Low-temperature spin-state transition in  $\text{LaCoO}_3$  investigated using resonant x-ray absorption at the Co K edge. *Phys. Rev. B* **73**, 054424 (2006).
2. de Groot, F. M. F. et al., Oxygen 1s X-ray-absorption edges of transition-metal oxides. *Phys. Rev. B* **40**, 5715-5723 (1989).
3. Ravel, B. & Newville, M., ATHENA, ARTEMIS, HEPHAESTUS: data analysis for X-ray absorption spectroscopy using IFEFFIT. *J. Synchrot. Radiat.* **12**, 537-541 (2005).
4. Tyson, T. A. et al., Valence state of Mn in Ca-doped  $\text{LaMnO}_3$  studied by high-resolution Mn K-beta emission spectroscopy. *Phys. Rev. B* **60**, 4665-4674 (1999).
5. Croft, M. et al., Systematic Mn *d*-configuration change in the  $\text{La}_{1-x}\text{Ca}_x\text{MnO}_3$  system: A Mn K-edge XAS study. *Phys. Rev. B* **55**, 8726-8732 (1997).
6. Ritter, C. et al., Influence of oxygen content on the structural, magnetotransport, and magnetic properties of  $\text{LaMnO}_{3+\delta}$ . *Phys. Rev. B* **56**, 8902-8911 (1997).
7. Yan, J. Q., Zhou, J. S., & Goodenough, J. B., Ferromagnetism in  $\text{LaCoO}_3$ . *Phys. Rev. B* **70**, 014402 (2004).
8. Takeda, T., Watanabe, H., & Yamaguchi, Y., Magnetic Structure of  $\text{SrCoO}_{2.5}$ . *J. Phys. Soc. Jpn.* **33**, 970-& (1972).
9. Arcon, I., Mirtic, B., & Kodre, A., Determination of valence states of chromium in calcium chromates by using X-ray absorption near-edge structure (XANES) spectroscopy. *J. Am. Ceram. Soc.* **81**, 222-224 (1998).
10. Russo, U. et al., Local interactions and electronic phenomena in substituted  $\text{LaFeO}_3$  perovskites. *Solid State Ionics* **176**, 97-102 (2005).
11. Yan, J. Q., Zhou, J. S., & Goodenough, J. B., Bond-length fluctuations and the spin-state transition in  $\text{LCoO}_3$  (L=La, Pr, and Nd). *Phys. Rev. B* **69**, 134409 (2004).
12. Medarde, M. L., Structural, magnetic and electronic properties of  $\text{RNiO}_3$  perovskites (R equals rare earth). *J Phys-Condens Mat* **9**, 1679-1707 (1997).

13. Zhou, J. S. et al., Enhanced susceptibility in  $\text{LNiO}_3$  perovskites ( $\text{L} = \text{La, Pr, Nd, Nd}_{0.5}\text{Sm}_{0.5}$ ). *Phys. Rev. Lett.* **84**, 526-529 (2000).
14. Suntivich, J., Gasteiger, H. A., Yabuuchi, N., & Shao-horn, Y., Electrocatalytic measurement methodology of oxide catalysts using a thin-film rotating disk electrode. *J. Electrochem. Soc.* **157**, B1263-B1268 (2010).